Dalton Transactions

ROYAL SOCIETY OF CHEMISTRY

PAPER

View Article Online
View Journal | View Issue

Cite this: *Dalton Trans.*, 2026, **55**, 5180

Oxygen vacancies as electronic bridges to reinforce Ru–TiO_2 metal–support interactions toward efficient electrocatalytic acidic hydrogen evolution

Wanjing Lai,[a,b,c] Xiao Yang,[a,c] Hailin Jiang,[a,c] Xuan Luo,[a,c] Jianwei Chen,[a,c] Shuwen Zhao,[a,c] Yanan Sun,[a,c] Linjie Zhang, *[a,b,c] Lei Yang*[d] and Lili Han *[a,b,c]

The development of hydrogen evolution reaction (HER) electrocatalysts that combine high activity, low cost, and long-term stability is crucial for advancing zero-carbon hydrogen energy technologies. Ru, with a 4d electronic structure similar to Pt and a comparatively lower cost, represents a highly promising alternative catalyst. However, its practical application is limited by challenges such as susceptibility to oxidation in acidic media and overly strong hydrogen adsorption. Here, we report a strong metal–support interaction (SMSI) strategy to construct Ru nanoparticles anchored on an oxygen-deficient TiO_{2-x} support (Ru/TiO_{2-x}), where oxygen vacancies function as electronic bridges to regulate interfacial electron transfer. In 0.5 M H_2SO_4 electrolyte, Ru/TiO_{2-x} achieves a current density of 10 mA cm^{-2} at an ultralow overpotential of 11 mV and retains nearly unchanged activity over 350 h of continuous operation. Combined systematic characterization and density functional theory calculations reveal that oxygen vacancies serve as electron donors, facilitating electron transfer from the TiO_{2-x} support to Ru. This electron redistribution downshifts the d-band center of Ru, thereby optimizing the hydrogen adsorption energy. By clarifying the role of defect-engineered SMSI in modulating the electronic structure and catalytic behavior of Ru, this work provides a rational material design strategy for developing highly efficient and stable Ru-based HER electrocatalysts.

Received 22nd January 2026,
Accepted 3rd March 2026

DOI: 10.1039/d6dt00176a

rsc.li/dalton

Introduction

Environmental pollution stemming from the heavy dependence on conventional fossil fuels has become ever more acute, driven by rapid global industrialization and continually expanding production capacity.[1,2] Developing and utilizing hydrogen energy, a renewable, zero-pollution, and high-energy-density alternative to fossil fuels, represents a highly viable pathway. Among various hydrogen production methods, water electrolysis powered by renewable electricity stands out for its environmental benefits and ability to produce high-purity hydrogen (H_2).[3–6] The overall water-splitting process consists of two half-reactions: the oxygen evolution reaction (OER) at the anode and the hydrogen evolution reaction (HER) at the cathode.[7–10] At the cathode, the HER involves proton reduction to form adsorbed hydrogen intermediates (*H), followed by their combination to generate molecular H_2.[11,12] This multiple process generally includes water adsorption on the electrode surface, water dissociation, and *H adsorption, each of which contributes to additional energy barriers.[13] The rational design of efficient electrocatalysts can effectively lower the activation energies associated with these elementary steps, thereby reducing the overall energy consumption. Therefore, the development of HER catalysts that simultaneously balance cost, catalytic activity, and long-term stability is essential for the industrial implementation of hydrogen energy technologies.[14–22]

Among the various HER catalysts, platinum (Pt)-based materials exhibit excellent intrinsic activity due to their unique electronic structure, which affords a near-optimal adsorption energy for hydrogen intermediates.[23–26] However, even the widely marketed commercial Pt/C catalyst still requires an overpotential of approximately 30 mV to reach a current density of 10 mA cm^{-2} in acidic electrolytes. Therefore, there is still a need to develop HER electrocatalysts with superior

[a]*State Key Laboratory of Structural Chemistry, Fujian Institute of Research on the Structure of Matter, Chinese Academy of Sciences, Fuzhou 350002, China. E-mail: zhanglinjie@fjirsm.ac.cn, llhan@fjirsm.ac.cn*
[b]*College of Chemistry, Fujian Normal University, Fuzhou 350108, China*
[c]*Fujian College, University of Chinese Academy of Sciences, Fuzhou 350002, China*
[d]*Ecological Environment Monitoring and Scientific Research Center, Taihu Basin & East China Sea Ecological Environment Supervision and Administration Bureau, Ministry of Ecology and Environment, Shanghai 200125, China. E-mail: yl198612@163.com*

activity, reduced cost, and enhanced stability through various strategies to further advance their practical application in large-scale water electrolysis for H_2 production.[27–30] Compared with the benchmark HER catalyst Pt, ruthenium (Ru) is less expensive (about one-third the price of Pt) and has a 4d electronic orbital structure similar to Pt, endowing it with excellent intrinsic HER activity and making it one of the most promising noble metal alternatives to Pt. However, Ru suffers from critical challenges, including susceptibility to over-oxidation under operating conditions, which can induce dissolution and catalytic deactivation, and its strong adsorption of *H under certain conditions can restrict H_2 desorption and compromise overall reaction kinetics. Therefore, optimization of the electronic structure of Ru-based catalysts through rational material design, together with concurrent enhancement of their stability, has become a central challenge of current research.[31,32]

In recent years, various strategies such as alloying, nanoengineering, interface engineering, and support modulation have been developed to tune the electronic structure of metals. For example, Chen *et al.* reported an Mn-doped CoO system in which Mn induces a high-spin to low-spin transition of Co^{2+}, accelerating the reconstruction of CoOOH active species.[33] Although this spin-state engineering strategy significantly improves the performance, its mechanism relies on complex spin coupling and orbital filling analysis and has not been demonstrated for acidic HER systems. Similarly, Cai *et al.* developed a Pt cluster catalyst (PtNC/Ni-CNTs/NCF) based on the wall-embedded geometric confinement strategy.[34] By embedding Pt nanoclusters into an N-doped carbon nanotube support, the electronic metal–support interaction between Pt and Ni optimizes the free energy of hydrogen adsorption, showing excellent performance under both acidic and basic HER conditions. However, this strategy mainly relies on the electronic synergistic effect between Pt and Ni bimetallic components. Zhang *et al.* regulated the degree of electron delocalization of Ni active sites in spinel $NiCo_2O_4$ catalysts through an anion substitution strategy (phosphorus doping), which in turn affected the active sites and product selectivity. This synthesis strategy, which optimizes the reaction path and product selectivity by adjusting the electronic structure of the active center, provides a new regulation idea for designing efficient catalysts for the HER.[35] Among these, strategies based on strong metal–support interactions (SMSI) have garnered significant attention for their ability to simultaneously optimize catalytic activity and stability.[36,37] The SMSI effect modulates the d-band center of Ru through electron transfer and interfacial interactions between the support and the metal, optimizing the adsorption free energy of *H and enhancing intrinsic activity.[38,39] At the same time, this strong interaction stabilizes Ru active sites, preventing their migration, aggregation, or dissolution during reactions, thereby significantly improving catalyst durability. Additionally, introducing defect structures such as oxygen, sulfur, or nitrogen vacancies can markedly alter the electronic properties of the support and its interaction with metal active centers. These vacancy defects not only serve as active sites for electronic modulation, enhancing electron transfer from the support to the metal, but also optimize the adsorption behavior of reaction intermediates on the catalyst surface, further improving HER performance.[40–42]

In this work, we constructed a vacancy-modified Ru nanoparticle catalyst system (Ru/TiO_{2-x}) on a reducible TiO_2 support for an efficient electrocatalytic HER in acidic media. Electrochemical tests demonstrate that the optimized Ru/TiO_{2-x} catalyst exhibits outstanding HER activity, requiring an overpotential of only 11 mV at 10 mA cm^{-2} while retaining more than 95% of its initial activity after 300 h of continuous operation. Further density functional theory calculations reveal that oxygen vacancies can function as electronic bridges to induce efficient interfacial electron redistribution between Ru nanoparticles and the TiO_{2-x} support, thereby enhancing electron transfer from the support to Ru and effectively modulating the d-band center of Ru to achieve favorable *H adsorption free energy. Concurrently, such electronic bridges strengthen the anchoring of Ru nanoparticles to the support, preventing detachment and aggregation of active components during reactions. This study highlights the potential of vacancy engineering to modulate strong metal–support interactions and establishes an effective strategy for designing high-performance and durable Ru-based catalysts for the HER.

Experimental section

Materials

All chemicals were obtained commercially and used as received without further purification. Titanium tetrachloride ($TiCl_4$, 99.6%), ethylene glycol ($C_2H_6O_2$, AR), ruthenium trichloride hydrate ($RuCl_3{\cdot}3H_2O$, >99.0%), and ethanol (C_2H_5OH, 99.7%) were purchased from J&K Co., Ltd. The commercial Pt/C catalyst (SPT20X, 20 wt%) was purchased from Suzhou Sinero Technology Co., Ltd. Hydrophilic carbon paper (HCP030N) was acquired from Shanghai Hesen Electric Co., Ltd. Nafion solution ($C_9HF_{17}O_5S$, 5wt%) was supplied by DuPont (China) Co., Ltd. Deionized water used throughout all experiments was obtained from a Millipore ultrapure water purification system.

Synthesis of TiO_2

Briefly, 60 mL of ethylene glycol was mixed with 2 mL of $TiCl_4$ solution under stirring for 5 min to obtain a homogeneous solution. Subsequently, 2 mL of deionized water was rapidly added, and the mixture was stirred for an additional 30 min. The resulting light-yellow solution was transferred into a 100 mL Teflon-lined stainless steel autoclave and heated at 140 °C for 12 h. After cooling to room temperature, the product was collected and repeatedly washed with deionized water and ethanol by centrifugation, followed by drying in a vacuum oven at 60 °C overnight to obtain the TiO_2 powder.

Synthesis of Ru/TiO_{2-x}

Defective TiO_{2-x} was first prepared by placing the as-synthesized TiO_2 powder in a tube furnace and annealing it at

250 °C for 1 h under a 5% H_2/95% Ar atmosphere. The resulting light gray TiO_{2-x} powder contained oxygen vacancies. Subsequently, 50 mg of TiO_{2-x} was dispersed in 50 mL of deionized water, stirred for 10 min, and ultrasonicated for 30 min to ensure complete dispersion. Then, 2 mL of an aqueous $RuCl_3{\cdot}3H_2O$ solution (20 mg L^{-1}) was added dropwise at room temperature under stirring, followed by an additional 1 h of ultrasonication. The suspension was transferred to a heating and stirring apparatus and maintained at 95 °C until complete solvent evaporation, yielding a gray–black solid. This precursor was placed in a ceramic crucible and reduced at 500 °C for 2 h under flowing 5% H_2/95% Ar at a heating rate of 2 °C min^{-1}. After natural cooling, the product was washed three times with deionized water and ethanol *via* centrifugation and dried overnight in a vacuum oven at 60 °C to obtain the final Ru/TiO_{2-x} catalyst.

Synthesis of Ru/TiO_2

To prepare the Ru/TiO_2 sample without oxygen vacancies as a control, the Ru/TiO_{2-x} catalyst was subsequently annealed in air at 200 °C for 2 h.

Characterization

X-ray diffraction (XRD) patterns were collected using an Ultima-IV X-ray diffractometer with a scanning rate of 5° min^{-1} and a scanning range of 5°–85°. Raman spectra were obtained using a HORIBA HR Evolution Raman spectrometer with a 532 nm laser as the excitation source. Electron paramagnetic resonance (EPR) measurements were carried out at 300 K using an ELEXSYS-II E500 spectrometer. The surface morphology and distribution of the materials were examined using a scanning electron microscope (SEM), specifically a Thermo Scientific Apreo 2 SEM, with the following settings: an accelerating voltage of 10 kV, a working distance of 8 mm, and a probe current of 5 pA. The sample morphology and structure were characterized by transmission electron microscopy (TEM) using a JEOL F200 microscope operating at 200 kV, integrated with an energy-dispersive spectroscopy (EDS) system for compositional analysis. X-ray photoelectron spectroscopy (XPS, ESCALAB 250 Xi) was employed to analyze the chemical states of different elements on the compound surfaces, with the C 1s peak (284.8 eV) used as the reference for binding energy calibration. The metal content in the catalyst was determined using a PerkinElmer Optima 5300DV ICP instrument.

Electrochemical measurements

The catalyst ink was prepared by ultrasonically dispersing 5 mg of Ru/TiO_{2-x} catalyst powder in 280 μL of water, 700 μL of ethanol, and 20 μL of 5% Nafion solution. 200 μL of the well-dispersed ink was added dropwise onto a hydrophilic carbon paper to achieve a loading of 1 mg cm^{-2} (based on ICP results and nominal compositions, the corresponding metal loadings were 0.0848 mg_{Ru} cm^{-2} for Ru/TiO_{2-x}, 0.073 mg_{Ru} cm^{-2} for Ru/TiO_2, and 0.2 mg_{Pt} cm^{-2} for Pt/C), followed by natural drying at room temperature. In a standard three-electrode system, this catalyst-coated carbon paper was used directly as the working electrode, while graphite rods were used as the counter electrode and Hg/Hg_2SO_4 was used as the reference electrode. The performance test was carried out in 0.5 M H_2SO_4 electrolyte saturated with N_2 using a CHI760 electrochemical workstation. CV tests were performed at 50 mV s^{-1}, and LSV measurements at 5 mV s^{-1}. All LSV curves were automatically compensated by 90% IR by the workstation. The same preparation and testing protocol was applied to all catalysts unless otherwise specified.

Theoretical calculations

Density functional theory (DFT) calculations were performed using the Vienna *Ab initio* Simulation Package (VASP) on Hygon 7495 central processing unit (CPU). The exchange–correlation energy was treated within the generalized gradient approximation (GGA) using the Perdew–Burke–Ernzerhof (PBE) functional. The interaction between valence electrons and ionic cores was described by the projector augmented-wave (PAW) method. Dispersion interactions were accounted for using the DFT-D3 method with Becke–Johnson damping (D3(BJ)). Plane-wave basis sets with a kinetic energy cutoff of 400 eV were used for geometry optimization, whereas static single-point calculations (*e.g.*, charge-density analyses) used an increased cutoff of 600 eV. Brillouin-zone integrations employed Monkhorst–Pack *k*-point meshes of 3 × 3 × 1 for structural relaxations and 11 × 11 × 1 for static calculations. The electronic self-consistency convergence criteria (EDIFF) were set to 1×10^{-5} eV for geometry optimization and 1×10^{-6} eV for static calculations. Structural optimization was carried out using the conjugate-gradient algorithm until the residual forces on each atom were below 0.02 eV $Å^{-1}$. Spin polarization was included in all calculations.

Results and discussion

Fig. 1a schematically illustrates the synthesis procedure of the Ru/TiO_{2-x} catalyst. First, white TiO_2 nanorod powders were synthesized using a conventional hydrothermal method reported previously (Fig. S1 and S2).[43] The synthesized TiO_2 powders were then treated at 250 °C for 1 h under a 5% H_2/95% Ar atmosphere. Through this pyrolytic reduction strategy, oxygen vacancy (O_v) defect-rich TiO_{2-x} was obtained (Fig. S3). Subsequently, TiO_{2-x} was uniformly dispersed in, followed by the dropwise addition of an aqueous $RuCl_3{\cdot}3H_2O$ solution under continuous stirring. The mixed solution was heated at 95 °C until complete solvent evaporation, producing a black-gray Ru/TiO_{2-x} precursor (Fig. S4). Finally, Ru/TiO_{2-x} was further annealed at 500 °C for 2 h under a 5% H_2/95% Ar atmosphere, then washed with water and ethanol *via* centrifugation to remove surface impurities, and dried to obtain the final Ru/TiO_{2-x} catalyst. For comparison, Ru/TiO_2 without O_v was synthesized by annealing under an air atmosphere as the control sample (Fig. S5). It is worth noting that this synthetic method is simple and easy to operate, featuring a short synthetic cycle and a high yield and excellent reproducibility. The

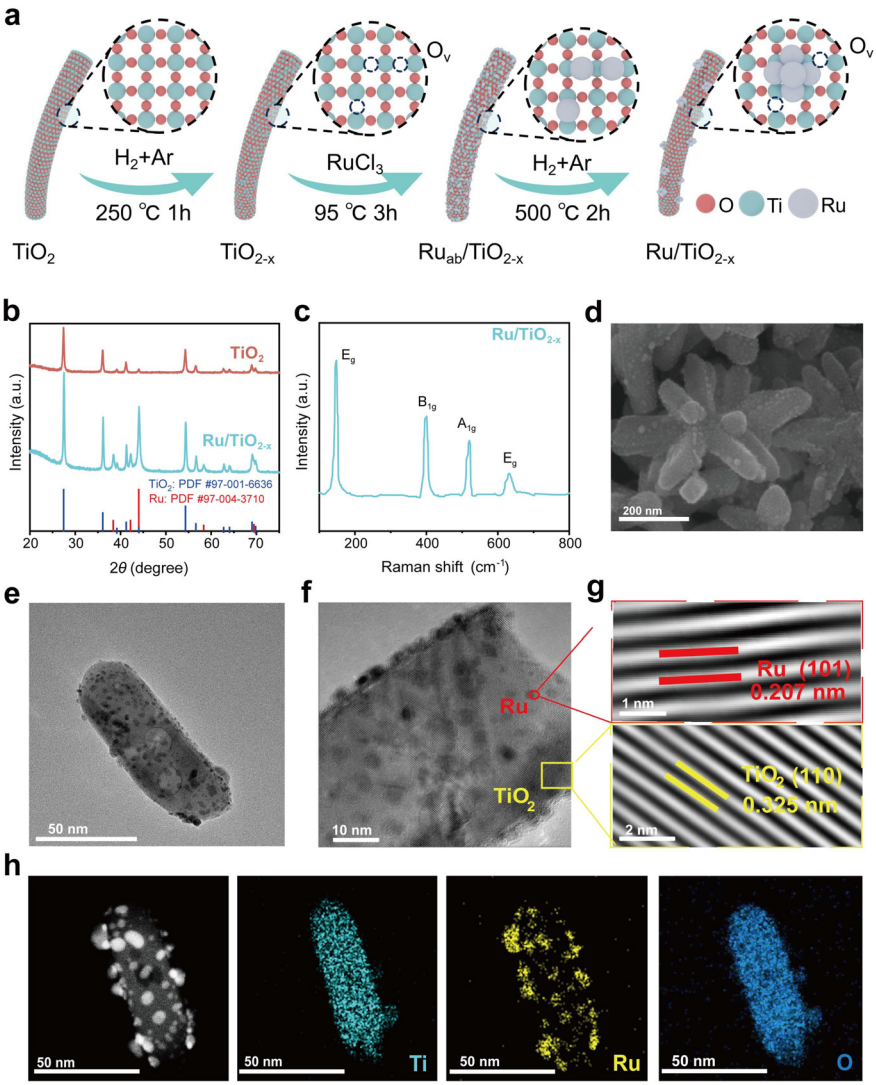

Fig. 1 (a) Schematic synthesis of Ru/TiO_{2-x}. (b) XRD patterns of TiO_2 and Ru/TiO_{2-x}. (c) Raman spectra of Ru/TiO_{2-x}. (d) SEM and (e) TEM images of Ru/TiO_{2-x}. (f) High magnification lattice fringe image of Ru/TiO_{2-x}; the red circle and yellow rectangle regions represent Ru particles and the TiO_{2-x} support, respectively. (g) Lattice fringe analysis of Ru particles and the TiO_{2-x} support in Ru/TiO_{2-x}. (h) HAADF-STEM and EDS mapping of Ru/TiO_{2-x}.

crystalline structure of the synthesized material was first analyzed by powder X-ray diffraction (XRD). As shown in Fig. 1b, the diffraction peaks at 27.43°, 36.08°, and 39.19° correspond to the (110), (101), and (200) planes of tetragonal TiO_2 (JCPDF-no. 97-001-6636), respectively. Raman spectroscopy was further employed to probe the phase structure (Fig. 1c). The four characteristic peaks at 147 cm^{-1}, 396 cm^{-1}, 519 cm^{-1}, and 628 cm^{-1} correspond to the E_g, B_{1g}, A_{1g}, and E_g vibrational modes of the α-phase TiO_2, confirming the presence of the typical anatase TiO_2 phase, consistent with the XRD results.[44,45] In addition, diffraction peaks at 38.38° and 42.19° can be assigned to the (100) and (002) planes of metallic Ru (JCPDF-no. 97-004-3710), indicating the successful deposition and preparation of Ru nanoparticles (NPs) on the TiO_{2-x} support. The morphology and microstructure of Ru/TiO_{2-x} were further investigated by electron microscopy. The scanning electron microscopy (SEM) image revealed large-area and uniformly ordered nanorod arrays of Ru/TiO_{2-x}, with Ru NPs clearly visible and uniformly distributed on their roughened surface (Fig. 1d), whereas pristine TiO_2 generally exhibits a clean and smooth surface (Fig. S6). The transmission electron microscopy (TEM) image confirmed that the Ru/TiO_{2-x} nanorods possessed a nanorod morphology with an average length of approximately 160 nm and a diameter of about 60 nm (Fig. 1e). Further high-resolution TEM (HRTEM) image analysis revealed lattice spacings of 0.325, 0.2499, and 0.228 nm, corresponding to the (110), (101), and (200) planes of TiO_2, along with lattice spacings of 0.207, 0.213 and 0.234 nm corresponding to the (101), (002) and (100) planes of Ru NPs (Fig. 1f and g, S7 and S8). These observations are fully consistent with the XRD results. Elemental mapping through energy-dispersive X-ray spectroscopy (EDX) showed that Ti, Ru, and O

elements are evenly distributed throughout the nanorod architecture (Fig. 1h). The precise metal contents were determined by inductively coupled plasma mass spectrometry (ICP-OES), yielding Ti and Ru mass fractions of 54.86 wt% and 8.48 wt%, respectively (Table S1). These analysis results confirm the successful and uniform loading of Ru NPs on the TiO_{2-x} support.

To study the impact of oxygen vacancies on the valence state and chemical environments of the constituent elements, X-ray photoelectron spectroscopy (XPS) measurements were further conducted. The survey spectrum clearly showed the presence of Ti, Ru, and O signals, indicating that Ru NPs were successfully loaded onto the TiO_{2-x} support (Fig. S9). In the high-resolution Ti 2p region, the coexistence of Ti 2p and Ru 3p was observed (Fig. 2a). Compared with Ru/TiO_2, the Ti $2p_{3/2}$ peak of Ru/TiO_{2-x} shifted by 0.20 eV toward lower binding energy, indicative of the generation of oxygen vacancies in the TiO_{2-x} support. Meanwhile, in Ru/TiO_{2-x}, the peak at 461.12 eV can be assigned to Ru $3p_{3/2}$, which displayed a pronounced negative shift of 0.73 eV compared to that of Ru/TiO_2, suggesting electron enrichment of Ru induced by the oxygen-deficient TiO_{2-x} support.[46,47] In addition, the high-resolution Ru 3d spectrum clearly revealed a higher proportion of Ru0 species in Ru/TiO_{2-x} compared with Ru/TiO_2 (Fig. 2b), further demonstrating that the oxygen-vacancy-rich TiO_{2-x} support significantly modulates the electronic structure of Ru.[48] As presented in Fig. 2c, the deconvolution of O 1s XPS indicated a substantially higher concentration of oxygen vacancies in Ru/TiO_{2-x} (27.18%) than in Ru/TiO_2 (17.18%). To further corroborate the presence of oxygen vacancies, electron paramagnetic resonance (EPR), which is sensitive to unpaired electrons, was employed. As shown in Fig. 2d, characteristic signals of oxygen vacancies were clearly detected in both Ru/TiO_{2-x} and TiO_{2-x},

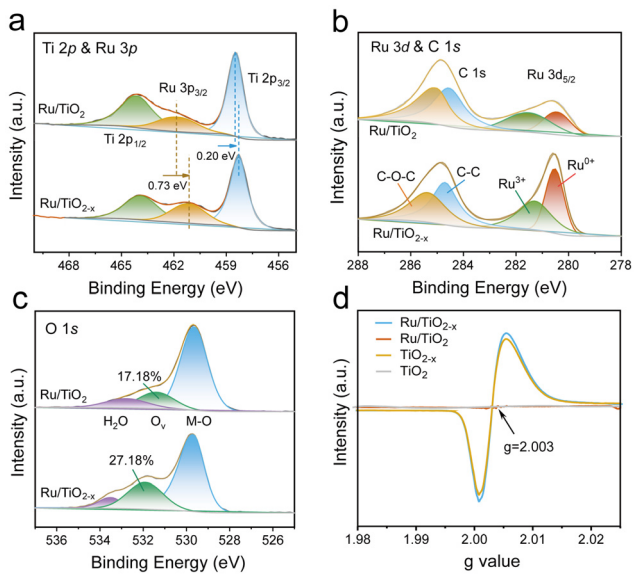

Fig. 2 (a) Ti 2p and Ru 3p XPS, (b) Ru 3d and C 1s XPS, and (c) O 1s XPS of Ru/TiO_2 and Ru/TiO_{2-x}. (d) EPR spectra of Ru/TiO_{2-x}, Ru/TiO_2, TiO_{2-x} and TiO_2.

confirming the successful construction of an oxygen vacancy-enriched TiO_{2-x} support. The presence of abundant oxygen vacancies further supports their role as electronic bridges facilitating interfacial electron transport. The above characterization results demonstrate that the target Ru/TiO_{2-x} catalyst was successfully prepared and that the oxygen vacancy-rich support effectively tailors the local electronic structure of Ru through strong metal–support interactions.[49–51]

To evaluate the electrocatalytic acidic HER performance of Ru/TiO_{2-x}, all electrochemical measurements were performed in a standard three-electrode configuration using N_2-saturated 0.5 M H_2SO_4 as the electrolyte. The catalyst-coated carbon paper served as the working electrode, a graphite rod was used as the counter electrode, and a Hg/Hg_2SO_4 electrode as the reference electrode. Fig. 3a shows the HER polarization curves of the catalysts Ru/TiO_{2-x}, Ru/TiO_2, TiO_2, TiO_{2-x} and commercial Pt/C. Among all tested catalysts, Ru/TiO_{2-x} exhibited the highest HER catalytic activity, delivering a current density of 10 mA cm^{-2} at an ultralow overpotential of only 11 mV, which is significantly lower than those of Ru/TiO_2 (112 mV) and commercial Pt/C catalysts (24 mV). These results preliminarily demonstrated the beneficial role of oxygen vacancies in enhancing catalytic performance. Notably, even at a high current density of 100 mA cm^{-2}, Ru/TiO_{2-x} maintains a low overpotential of 97 mV, outperforming Ru/TiO_2 (226 mV) and Pt/C (108 mV) (Fig. 3b). To further elucidate the reaction kinetics, the polarization curves were analyzed using Tafel plots (Fig. 3c). The results showed that the Tafel slope of Ru/TiO_{2-x} was as low as 43.22 mV dec^{-1}, although slightly higher than that of commercial Pt/C (28.94 mV dec^{-1}), but significantly lower than those of TiO_2 (302.57 mV dec^{-1}), TiO_{2-x} (140.07 mV dec^{-1}) and Ru/TiO_2 (95.54 mV dec^{-1}), indicating more favorable HER kinetics on the oxygen vacancy-engineered Ru/TiO_{2-x} catalyst.[52]

In addition to the polarization behavior and kinetic parameters, electrochemical impedance spectroscopy (EIS) provided further insights into the interfacial charge-transfer properties. As shown in Fig. 3d, Ru/TiO_{2-x} exhibited the smallest charge transfer resistance (R_{ct}), indicating the most efficient electron transfer at the electrode–electrolyte interface. The minimized charge-transfer resistance can be attributed to oxygen vacancy-derived electronic bridges, which provide rapid electron transport pathways across the Ru/TiO_{2-x} interface. Moreover, Ru/TiO_{2-x} exhibited excellent mass activity (Fig. S10). Fig. 3e compares the mass activities of different catalysts at overpotentials of 75, 100, and 200 mV, respectively. Notably, Ru/TiO_{2-x} achieves a high mass activity of 2.281 A mg^{-1} at an overpotential of 200 mV, which is 2.57 times and 5.23 times that of Pt/C (0.888 A mg^{-1}) and Ru/TiO_2 (0.436 A mg^{-1}), respectively. This enhanced mass activity further reflects the effectiveness of the electron bridge in maximizing the utilization efficiency of Ru active sites. To further identify the intrinsic origin of the enhanced HER activity, the copper underpotential deposition (Cu-upd) and hydrogen underpotential deposition (H-upd) methods were adopted to evaluate the electrochemically active surface area (ECSA) values of the Ru-

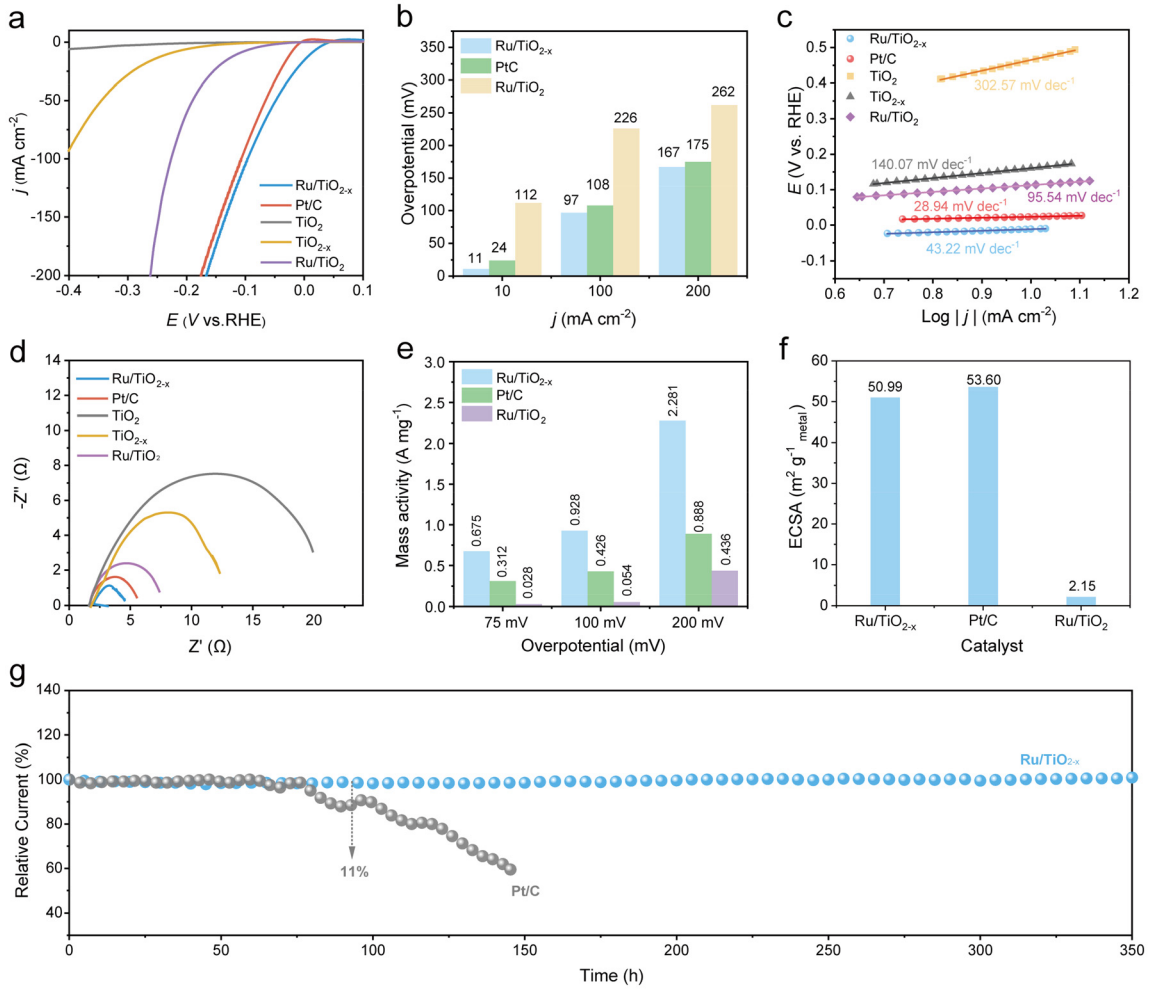

Fig. 3 (a) HER polarization curves of Ru/TiO_{2-x}, Ru/TiO_2, TiO_2, TiO_{2-x} and Pt/C. (b) Comparison of overpotentials of Ru/TiO_{2-x}, Ru/TiO_2 and Pt/C at different current densities. (c) Tafel plots of Ru/TiO_{2-x}, Ru/TiO_2, TiO_2, TiO_{2-x} and Pt/C. (d) EIS Nyquist plots of Ru/TiO_{2-x}, Ru/TiO_2, TiO_2, TiO_{2-x} and Pt/C. (e) Mass activity of Ru/TiO_{2-x}, Ru/TiO_2, TiO_2, TiO_{2-x} and Pt/C at different overpotentials. (f) Electrochemically active surface area (ECSA) values of Ru/TiO_{2-x}, Ru/TiO_2, and Pt/C. (g) Comparison of the stability of Ru/TiO_{2-x} and Pt/C at 10 mA cm^{-2}.

based and Pt/C catalysts, respectively (Fig. S11). As shown in Fig. 3f, the calculated ECSA value of Ru/TiO_{2-x} is 50.99 m^2 g^{-1}, which is comparable to that of commercial Pt/C (53.60 m^2 g^{-1}), providing compelling evidence for its excellent activity. Finally, the long-term stability of Ru/TiO_{2-x} was evaluated by chronopotentiometry at a constant current density of 10 mA cm^{-2}. As shown in Fig. 3g, Ru/TiO_{2-x} maintained stable catalytic activity over 350 h of continuous testing without significant attenuation, whereas commercial Pt/C showed a significant decrease in activity after 100 h. To further verify the structural stability, post-stability TEM characterization studies of Ru/TiO_{2-x} revealed that its microstructure did not change significantly and its original morphological characteristics were maintained (Fig. S12–S14). Meanwhile, XPS and EPR tests confirmed that the valence states and oxygen vacancy content were basically the same as those of the fresh sample, further indicating the excellent structural stability of Ru/TiO_{2-x} during the reaction (Fig. S15). Collectively, these results unequivocally demonstrate that the oxygen vacancy-engineered Ru/TiO_{2-x} catalyst possesses both excellent catalytic activity and structural stability for acidic HER. Besides acidic HER, the performance of Ru/TiO_{2-x} in 1 M KOH alkaline medium was also explored (Fig. S16). The results revealed an overpotential of 24 mV at a current density of 10 mA cm^{-2} and a Tafel slope of 35.89 mV dec^{-1}, which are lower than those of commercial Pt/C (34 mV and 47.38 mV dec^{-1}), indicating more favorable reaction kinetics. In addition, the consistently higher mass activity than that of commercial Pt/C at the same potential was also verified. These results demonstrate that the Ru/TiO_{2-x} catalyst maintains excellent catalytic performance across both acidic and alkaline environments, further confirming its robust and versatile HER activity.

Density functional theory (DFT) calculations were performed to gain in-depth insights into the influence of the oxygen vacancy-rich TiO_{2-x} support on the electronic structure of Ru NPs and to elucidate the microscopic origin of the superior HER performance of Ru/TiO_{2-x}. Based on the previous HRTEM analysis results, the (002) facet of TiO_2 and the

(101) facet of Ru were selected as the exposed facets to construct four representative structural models: pristine TiO_2 without oxygen vacancies, TiO_{2-x} with oxygen vacancies, Ru/TiO_2 with Ru loaded on TiO_2 without oxygen vacancies, and Ru/TiO_{2-x} with Ru loaded on TiO_{2-x} with oxygen vacancies (Fig. 4a–d). The electronic interactions at the Ru–TiO_2 interface were first examined by differential charge density analysis. As shown in Fig. 4e, pronounced interfacial electron redistribution occurs upon contact between Ru and the TiO_2 or TiO_{2-x} support. Notably, the introduction of oxygen vacancies significantly strengthens the interfacial electron coupling, leading to enhanced electron accumulation at the Ru–TiO_2 interface (Fig. 4f). Electron localization function (ELF) analysis further reveals that, compared with the system without oxygen vacancies, the electrons around Ru in Ru/TiO_{2-x} exhibit more delocalized characteristics (Fig. 4g and h), confirming the formation of oxygen vacancy-mediated electronic bridges, which promote the interaction with *H intermediates during the HER. To further quantify the electronic structure modulation, density of states (DOS) calculations were conducted to determine the d-band centers of Ru in different systems (Fig. 4i and j, and S17). The calculated d-band centers (with respect to the Fermi level) show that the d-band center of Ru/TiO_2 is located at 0.127 eV, whereas that of Ru/TiO_{2-x} shifts downward to −0.105 eV. A higher d-band center generally corresponds to overly strong adsorption of *H intermediates, resulting in difficult H_2 desorption. By functioning as electronic bridges, the oxygen vacancies effectively enhance metal–support interactions between Ru and TiO_{2-x} within Ru/TiO_{2-x} and downshift the d-band center of Ru, thereby optimizing the adsorption strength of *H intermediates. This electronic regulation provides a rational explanation for the markedly improved

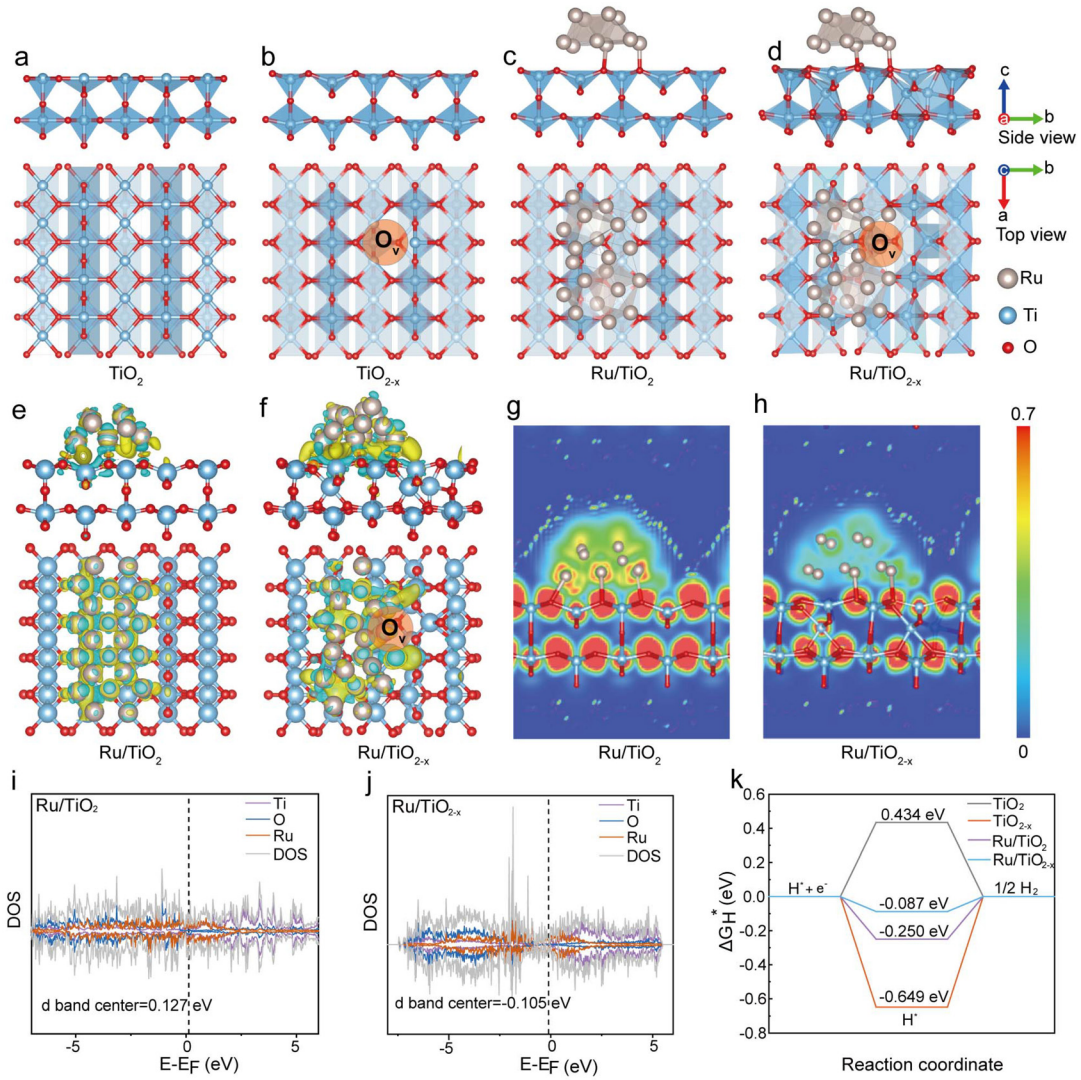

Fig. 4 Side and top views of four structural models: (a) TiO_2, (b) TiO_{2-x}, (c) Ru/TiO_2, and (d) Ru/TiO_{2-x}. Side and top views of the differential charge density distributions of (e) Ru/TiO_2 and (f) Ru/TiO_{2-x}. (g and h) 2D charge density distributions of Ru/TiO_2 and Ru/TiO_{2-x}. The DOS analysis of (i) Ru/TiO_2 and (j) Ru/TiO_{2-x}. (k) *H adsorption free energies of TiO_2, TiO_{2-x}, Ru/TiO_2 and Ru/TiO_{2-x}.

HER performance of Ru/TiO_{2-x} compared with Ru/TiO_2.[50] Furthermore, the Gibbs free energy of *H intermediate adsorption (ΔG_{*H}) was calculated to directly assess the HER thermodynamics. As depicted in Fig. 4k, Ru/TiO_{2-x} exhibits a ΔG_{*H} value closest to zero, indicating an optimal balance between *H adsorption and desorption, thus endowing it with excellent HER catalytic activity.[1,53] Overall, these theoretical results demonstrate that oxygen vacancies significantly enhance the electronic interaction between metallic Ru and the TiO_{2-x} support, inducing active site electronic delocalization and optimizing d-band centers, thereby improving the H_2 desorption ability of Ru/TiO_{2-x} and significantly enhancing its HER electrocatalytic performance.

Conclusions

In summary, an efficient Ru/TiO_{2-x} electrocatalyst was successfully developed by anchoring Ru nanoparticles on an oxygen vacancy-engineered TiO_2 support. Benefiting from the strong metal–support interaction induced by oxygen vacancy electronic bridges, the Ru/TiO_{2-x} catalyst delivers an ultralow overpotential of only 11 mV at a current density of 10 mA cm^{-2} for the HER in acidic media and maintains outstanding durability over 350 h of continuous operation at the same current density. Density functional theory calculations reveal that the superior HER performance of Ru/TiO_{2-x}, surpassing even that of commercial Pt/C, originates from oxygen vacancy-enhanced electronic coupling between Ru and the TiO_2 support. This interaction induces electron enrichment and delocalization at the Ru–support interface, effectively modulating the local electronic structure of Ru active sites. Consequently, the Ru d-band center is downshifted, optimizing *H intermediate adsorption strength and accelerating the reaction kinetics from *H adsorption to H_2 desorption. Overall, this work provides fundamental insights into oxygen vacancy-engineered strong metal–support interactions and offers a viable strategy for the rational design of highly efficient and durable Ru-based electrocatalysts for hydrogen evolution.

Author contributions

W. Lai: investigation, methodology, visualization, formal analysis, and writing – original draft. X. Yang: software and validation. H. Jiang: investigation and methodology. X. Luo: investigation and validation. J. Chen: visualization and formal analysis. S. Zhao: investigation and data curation. Y. Sun: validation. L. Zhang: conceptualization, writing – review & editing, and supervision. L. Yang: resources and writing – review & editing. L. Han: writing – review & editing, funding acquisition, and project administration.

Conflicts of interest

There are no conflicts to declare.

Data availability

The data supporting this article are available within the article and the supplementary information (SI). The supplementary information provides additional characterization data, including TEM images, XRD patterns, XPS spectrum, electrochemcial data, and the computational details (PDF). See DOI: https://doi.org/10.1039/d6dt00176a.

Acknowledgements

This work was supported by the National Key Research and Development Program of China (2022YFA1505700), the National Natural Science Foundation of China (22578449, 22475214 and 22205232), the Talent Plan of Shanghai Branch, Chinese Academy of Sciences (CASSHB-QNPD-2023-020), and the Natural Science Foundation of Fujian Province (2023J01213 and 2023J06044). The authors also gratefully acknowledge the Transmission Electron Microscope Platform of Fujian Science & Technology Innovation Laboratory for Optoelectronic Information of China and the computation facilities provided by HZWTECH.

References

1 H. Chen, Z. Gao, S. Ren, R. T. Gao, L. Wu and L. Wang, *Adv. Energy Mater.*, 2024, **15**, 2403067.
2 D. Guan, B. Wang, J. Zhang, R. Shi, K. Jiao, L. Li, Y. Wang, B. Xie, Q. Zhang, J. Yu, Y. Zhu, Z. Shao and M. Ni, *Energy Environ. Sci.*, 2023, **16**, 4926–4943.
3 S. Chen, X. Xiao, Z. Li and L. Ouyang, *Mater. Today*, 2025, **90**, 800–814.
4 M. Habibi, M. G. Hosseini and K. Wang, *Renewable Sustainable Energy Rev.*, 2026, **226**, 116193.
5 M. G. Gado, *Renewable Sustainable Energy Rev.*, 2026, **230**, 116683.
6 W. Jia, T. Ding and Y. He, *Renewable Sustainable Energy Rev.*, 2026, **226**, 116375.
7 J. Z. Yang, T. Y. Lam, Z. X. Luo, Q. Cheng, G. B. Wang and H. Yao, *Renewable Sustainable Energy*, 2025, **218**, 115804.
8 Z. Zhao, T. Chen, B. Ding, S. Zhang, D. Chen, G. Chen, Y. Zhu and X. Zhang, *Chem. Eng. J.*, 2025, **523**, 168834.
9 L. Liang, K.-Y. Niu, L. Zhang, J. Tian, K. Zhou, X.-L. Wang, X.-M. Zhang and M. Hong, *ACS Appl. Nano Mater.*, 2021, **4**, 6135–6144.
10 X. Huang, Y. Li, J. Cheng, Y. Xu, J. Zhu, R. Liu, Y. Xu, J. Zhao, K. Cheng and Z. Cao, *Chem. Eng. J.*, 2026, **527**, 171036.
11 J. M. Gisbert-González, C. G. Rodellar, J. Druce, E. Ortega, B. R. Cuenya and S. Z. Oener, *J. Am. Chem. Soc.*, 2025, **147**, 5472–5485.
12 T. Guo, C. Wang, L. Chen, G. Hu, J. Liu, G. Ren and Q. Guo, *Composites, Part B*, 2025, **305**, 112766.

13 M. N. Hossain, L. Zhang, R. Neagu and S. Sun, *Chem. Soc. Rev.*, 2025, **54**, 3323–3386.
14 J. Lin, X. Wang, Z. Zhao, D. Chen, R. Liu, Z. Ye, B. Lu, Y. Hou and J. Lu, *Carbon Energy*, 2024, **6**, E555.
15 C. Cai, H. Lee, W. Shi, Y. Liu, B. Zhang, L. Sun and T. Wang, *ACS Energy Lett.*, 2025, **10**, 1483–1490.
16 Q. Xie, L. Xiao, X. Zhao, Q. Liu and G. Hu, *Mater. Today*, 2025, **88**, 492–525.
17 M. Faizan, H. Bibi, E. Aamir, R. Saeed, T. S. Kiong and H. Song, *Renewable Sustainable Energy Rev.*, 2025, **212**, 115385.
18 A. Mathew, S. Rajendran, T. Mathew and N. R. Shiju, *EnergyChem*, 2025, **7**, 100161.
19 Y. Zhao, J. Huang, K. Zhang, Y. Li, Z. Ge, Y. Zheng, S. Ji, J. Lu, Y. Ren, C. Wu and M. Jin, *ACS Nano*, 2025, **19**, 25273–25283.
20 J. W. Lee, H. U. Din, T. Im, C. K. Hwang, J. M. Kim, J. H. Lee and S. Jeong, *Carbon Energy*, 2025, **7**, E720.
21 U. Arshad, J. Tang and Z. Shao, *SusMat*, 2025, **5**, e70013.
22 X. Gao, S. Dai, Y. Teng, Q. Wang, Z. Zhang, Z. Yang, M. Park, H. Wang, Z. Jia, Y. Wang and Y. Yang, *Nano-Micro Lett.*, 2024, **16**, 108.
23 J. Li, Y. Lv, X. Wu, X. Guo, Z. Yang, J. Guo, T. Zhou and D. Jia, *Chin. J. Catal.*, 2025, **69**, 203–218.
24 K. Dong, X. Li, S. Sidra, D. H. Kim, D. T. Tran, N. H. Kim and J. H. Lee, *Chem. Eng. J.*, 2025, **524**, 169674.
25 R. Wu, H. Liu, J. Xu, M. R. Qu, Y. Y. Qin, X. S. Zheng, J. F. Zhu, H. Li, X. Z. Su and S. H. Yu, *Adv. Energy Mater.*, 2025, **15**, 2405846.
26 X. Jiao, C. Ma, B. Huang, D. Zhao, F. Feng, S. Han, N. Yang, Q. Lu, Y. Ge and Q. Xu, *Adv. Powder Mater.*, 2025, **4**, 100320.
27 M. Smiljanić, M. Bele, L. Pavko, A. Hrnjić, F. Ruiz-Zepeda, L. Bijelić, A. R. Kamšek, M. Nuhanović, A. Marsel, L. Gašparič, A. Kokalj and N. Hodnik, *Chem. Eng. J.*, 2025, **517**, 164204.
28 X. Yang, C. Mu, Y. Jiang, X. Meng, Z. Tong and K. Huang, *Appl. Catal., B*, 2025, **379**, 125720.
29 Y. Kuang, F. Yang and L. Feng, *Adv. Energy Mater.*, 2024, **14**, 2402043.
30 C. Li, L. Chen, D. Dou, H. Wang, Q. Zhao and Y. Cong, *Ionics*, 2023, **29**, 4987–5001.
31 M. Kim, J. Park, H. Choi, S. Kim, I. Jang, H. Y. Kim, N. Jung, S. J. Yoo, J. T. Hupp and D. Whang, *Adv. Funct. Mater.*, 2025, **36**, e06866.
32 V. D. Quach, A. Harsan, M. C. Spadaro, M. Botifoll, J. Arbiol, M. Knezevic, C. Colbeau-Justin, F. Dumeignil, H. Vezin, R. Wojcieszak, T. Le Bahers, C. Michel and M. N. Ghazzal, *Adv. Sci.*, 2025, **12**, e01835.
33 Z.-Q. Chen, W.-J. Cai, H.-J. Zhang, K. Xiao, B. Huang and Z.-Q. Liu, *Chem. Sci.*, 2025, **16**, 14750–14759.
34 W.-J. Cai, Z.-Q. Chen, T. Ouyang, K. Xiao and Z.-Q. Liu, *ACS Nano*, 2025, **19**, 29554–29565.
35 H. J. Zhang, Z. Q. Chen, X. T. Ye, K. Xiao and Z. Q. Liu, *Angew. Chem., Int. Ed.*, 2024, **64**, e202421027.
36 Y. Yang, Z. Jia, Q. Wang, Y. Liu, L. Sun, B. Sun, J. Kuang, S. Dai, J. He, S. Liu, L. Duan, H. Tang, L.-C. Zhang, J. J. Kruzic, J. Lu and B. Shen, *Energy Environ. Sci.*, 2024, **17**, 5854–5865.
37 Q.-L. Ma, J. Wei, Z. Lin, Y. Guo, H. Tian, Q. Liu, H. Lin, P. Su and Y. Tang, *Appl. Catal., B*, 2025, **378**, 125547.
38 L. Liu, D. Li, H. Zhao, A. Dimitrova, L. Li, Y. Fang, S. Krischok, W. Shi and Y. Lei, *Appl. Catal., B*, 2019, **244**, 87–95.
39 C. Chong, S. K. Boong, T. R. Mogan, J. M. K. Loh, Y. Ni, S. Das, H. Li, H. Arandiyan, B. Wu and H. K. Lee, *Nano Energy*, 2026, **147**, 111574.
40 Y. Fu, H. Wang, N. Li, L. Mao, X. Wang, Q. Li and J. Qian, *Chin. Chem. Lett.*, 2025, **36**, 110890.
41 H. Wang, J. Liu, H. Ni, X. Wang, X. Zhu, Q. Li and J. Qian, *Sci. China Mater.*, 2025, **68**, 2327–2336.
42 X. Zhuge, C. Wang, Y. Li, Y. Zong, W. Xiao, D. Chen, J. Wang, T. Ma, M. Song, Z. Wu and L. Wang, *Sci. China Mater.*, 2025, **68**, 4471–4480.
43 M. Ge, Q. Li, C. Cao, J. Huang, S. Li, S. Zhang, Z. Chen, K. Zhang, S. S. Al-Deyab and Y. Lai, *Adv. Sci.*, 2016, **4**, 1600152.
44 L. Moriau, I. Marić, M. Bele, A. Logar, N. Hodnik and A. K. Surca, *Int. J. Hydrogen Energy*, 2025, **100**, 214–221.
45 Q. Cheng, Y.-J. Yuan, R. Tang, Q.-Y. Liu, L. Bao, P. Wang, J. Zhong, Z. Zhao, Z.-T. Yu and Z. Zou, *ACS Catal.*, 2022, **12**, 2118–2125.
46 E. Li, Y. Shen, Y. Li, Y. Zong, W. Xiao, G. Xu, J. Wang, H. Li, T. Ma, Z. Wu and L. Wang, *Appl. Catal., B*, 2026, **382**, 126022.
47 E. Liu, X. Wang, J. Li, C. Chen, Q. Li, X. Lv and J. Dang, *J. Mater. Sci. Technol.*, 2026, **254**, 71–80.
48 X. Fu, X. Huang, Y. Cen, X. Ren, L. Yan, S. Jin, Z. Zhuang, W. Li and S. Tian, *Small*, 2024, **20**, e2406387.
49 L.-N. Chen, S.-H. Wang, P.-Y. Zhang, Z.-X. Chen, X. Lin, H.-J. Yang, T. Sheng, W.-F. Lin, N. Tian, S.-G. Sun and Z.-Y. Zhou, *Nano Energy*, 2021, **88**, 106211.
50 S. Zhao, S.-F. Hung, L. Deng, W.-J. Zeng, T. Xiao, S. Li, C.-H. Kuo, H.-Y. Chen, F. Hu and S. Peng, *Nat. Commun.*, 2024, **15**, 2728.
51 D. Zhao, S. Lyu, Q. Cheng, Y. Liu, P. Zhao, Q. Zhang, Y. Zhang, Y. Pan, X. Li, S. Xiong, Z. Wang and X. Li, *J. Am. Chem. Soc.*, 2025, **147**, 20493–20503.
52 M. Smiljanić, S. Panić, M. Bele, F. Ruiz-Zepeda, L. Pavko, L. Gašparič, A. Kokalj, M. Gaberščcek and N. Hodnik, *ACS Catal.*, 2022, **12**, 13021–13033.
53 Z. Wu, P. Yang, Q. Li, W. Xiao, Z. Li, G. Xu, F. Liu, B. Jia, T. Ma, S. Feng and L. Wang, *Angew. Chem., Int. Ed.*, 2023, **62**, e202300406.